PHOTONICS Research

Circular Dammann gratings for enhanced control of the ring profile of perfect optical vortices

Junjie Yu,[1,5] Chaofeng Miao,[1,2,3] Jun Wu,[4] and Changhe Zhou[1,6]

[1]Laboratory of Information Optics and Opto-electronic Technology, Shanghai Institute of Optics and Fine Mechanics, Chinese Academy of Sciences, Shanghai 201800, China
[2]School of Physical Science and Technology, ShanghaiTech University, Shanghai 201210, China
[3]University of Chinese Academy of Sciences, Beijing 100049, China
[4]Department of Physics, Zhejiang University of Science and Technology, Hangzhou 310023, China
[5]e-mail: Junjiey@siom.ac.cn
[6]e-mail: chazhou@mail.shcnc.ac.cn

Received 9 January 2020; revised 6 March 2020; accepted 6 March 2020; posted 6 March 2020 (Doc. ID 387527); published 21 April 2020

Perfect optical vortices (POVs) provide a solution to address the challenge induced by strong dependence of classical optical vortices on their carried topological charges. However, traditional POVs are all shaped into bright rings with a single main lobe along the radial direction. Here we propose a method for enhanced control on the ring profile (the radial intensity profile of circular rings) of POVs based on modulated circular sine/cosine radial functions, which is realized by a circular Dammann grating embedded with a spiral phase. Specifically, a type of "absolute" dark POVs surrounded by two bright lobe rings in each side is presented, which provides a perfect annular potential well along those dark impulse rings for trapping low-index particles, cells, or quantum gases. In addition, several POVs with different ring profiles, including conventional POVs with bright rings, the dark POVs mentioned above, and also POVs with tunable ring profiles, are demonstrated. This work opens up new possibilities to controllably tune the ring profile of perfect vortices, and this type of generalized POVs will enrich the content of singular optics and expand the application scope of perfect vortices in a range of areas including optical manipulation, both quantum and classical optical communications, enhanced optical imaging, and also novel structured pumping lasers.

https://doi.org/10.1364/PRJ.387527

1. INTRODUCTION

An optical vortex is identified typically as a phase singularity encircled with helical wavefront, which contributes essentially to one of the important fundamentals of wave phenomena: any wave field containing phase singularities, not limited to optics, could carry orbital angular momentum (OAM) [1,2]. Due to its unique properties, including its carried OAM associated with doughnut-shaped profiles [3], optical vortices are arousing ever-increasing interest among both the scientific and engineering communities. In the past decades, the optical vortex had found exciting applications in a great variety of realms such as stimulated emission depletion (STED) nanoscopy [4,5], optical manipulation [6–8], both quantum and classical OAM-multiplexed optical communications [9–11], optical vortex coronagraphy [12], enhanced optical imaging [13,14], OAM-based radars [15], extreme-ultraviolet vortices [16,17], and recent high-intensity vortex physics [18–20]. Nowadays, the vortex is not limited to optical waves; it has been extended into other spectrum ranges, such as the X-ray [21], gamma-ray [22], and terahertz (THz)-ray [23,24] ranges, and also other waves including twisted electric beam waves [25,26] and acoustic vortices [27,28]. However, the size of the doughnut-shaped patterns generated by conventional vortices is strongly dependent on the carried topological charge, which hampers their applications in many practical fields. In 2013, Ostrvsky and coworkers [29] introduced the concept of perfect optical vortices (POVs), which are shaped into a thin ring with their radius being quasi-independent on the topological charge. Thanks to this unique property, the new type of optical vortices offers a possibility to couple multiple OAM beams into a certain fiber with a fixed annular index profile [30], and thus POVs are intriguing for their brilliant prospects for the application of OAM-multiplexed optical fiber communications. Also, this "perfect" vortex beam is of significant interest in dynamically trapping micro-particles, atoms, and quantum gases along those bright rings. It has been demonstrated that these POVs provide a possibility to transfer OAM to trapped particles along bright circular rings [31,32]. More importantly, the steady radial intensity profile and the independent ring diameter enable control of the rotation velocity of trapped particles along the same orbit just by changing the topological

charge. Recently, POVs were also explored for other different application purposes. Reddy *et al.* [33] demonstrated a type of non-diffracting speckles generated by scattering a POV beam through a rough surface. Zhang *et al.* [34] proposed a plasmonic structured illumination microscopy imaging technique with the use of POVs for enhancing the excitation efficiency of surface plasmons and reducing the background noise of the excited fluorescence. Also, POVs were employed for exploration of various nonlinear phenomena such as harmonic generation [35], parametric down-conversion [36], and perfect quantum optical vortex states [37]. Furthermore, a type of vectorial perfect vortices was proposed and demonstrated, which provides more degrees of freedom in beam manipulation [38–40]. Subsequently, the concept of POVs was generalized to a type of elliptical POVs, where those symmetrical circular rings were transformed into asymmetric elliptical rings [41,42].

However, those thin rings of POVs mentioned above are all bright rings, i.e., there is only a single main lobe in the intensity profile of the bright rings along the radial coordinate, and those bright rings could also hinder their applications in some scenarios. An important case, for instance, is that particles/cells will be difficult to trap along those bright rings generated by conventional POVs when their refractive index is lower than the surrounding medium. Recently, Liang *et al.* [43] proposed an interesting scheme for trapping the low-refractive-index particles with POVs, where the size of the trapped particles was comparable to the radius of the circular rings generated by those POVs. Moreover, a point trap was needed to improve the stability of the ring trap, and that composited trap could essentially be regarded as a dark ring constructed by the central point spot and the surrounding annular ring. Most recently, the same group [44] presented an attractive scheme for generation of a dark POV, termed double-ring POVs by them, through the use of the Fourier transform of azimuthal polarized Bessel beams, which could be regarded essentially as incoherent superposition of two opposite circularly polarized POVs. However, the sharpness of those dark POVs degenerated with the increase of topological charge.

In an ideal situation, the complex amplitude of a POV could be expressed by $\delta(\rho-\rho_0)\exp(il\varphi)$ [29], where $\delta(\cdot)$ denotes the Dirac delta function, (ρ,φ) are the radial and azimuthal coordinates, and ρ_0 is the ring radius of the POVs. This formula indicates that, similar to a spatial impulse, the ring width of the POVs could be infinitely thin and the ring brightness could be infinitely intense in theory. Actually, in the late 1990s, Amidror [45,46] called this spatial delta function in the two-dimensional (2D) case an impulse ring and pointed out that the Fourier spectrum of a 2D radially periodic function consists of half-order derivative impulse rings $\delta^{1/2}(\rho-\rho_0)$ when he investigated the spectrum of radially periodic images. Amidror's work became an important basic theory for the development of a novel diffractive optical element called circular Dammann gratings (CDGs), which was first proposed by Zhou *et al.* [47], about 10 years later [48,49]. In our previous paper [50], we demonstrated that a CDG could provide an effective method for generation of controllable impulse rings and predicted that this method could be used for generation of perfect vortices with a controllable ring profile, especially those dark POVs.

In this work, we propose a method for enhanced control of the ring profile (the intensity profile of impulse rings along the radial coordinate) of POVs based on modulated circular sine/cosine functions, which are realized by a CDG embedded with a spiral phase. Specifically, one could obtain a type of "absolute" dark perfect vortex rings surrounded by two bright lobe rings in each side by controlling the structure of the CDGs. This work opens up new possibilities to controllably tune the ring profile of POVs, and this type of generalized perfect vortices will enrich the content of singular optics and find applications in a variety of areas such as optical manipulations, quantum and classical optical communications, enhanced optical imaging, and also novel structured pumping lasers.

2. PRINCIPLE AND METHODS

A. Design Principle

It is well demonstrated that the transmission function of a circular grating could be decomposed into a series of circular sine or cosine functions with different radial frequencies, and it can be written as a sum of a Fourier series (or called a Hankel series) [45,46]. After a spiral phase is embedded, the transmission function can be written as

$$T(r,\theta)=T(r)\exp(il\theta)=\frac{a_0}{2}\exp(il\theta)+\sum_{m=1}^{\infty}a_m\cos\left(2\pi m\frac{r}{\Lambda}\right)\exp(il\theta), \quad (1)$$

where (r,θ) are the polar coordinates on the plane of a circular grating and the Fourier coefficient of the mth order a_m, with constant coefficients omitted, can be expressed by

$$a_m=\int_0^{\Lambda}T(r)\cos\left(2\pi m\frac{r}{\Lambda}\right)\mathrm{d}r. \quad (2)$$

The mth order of the Hankel series expressed in Eq. (1) can also be, according to Euler's formula, rewritten as

$$h_m(r,\theta)=\frac{a_m\exp(il\theta)}{2}\left[\exp\left(i2\pi m\frac{r}{\Lambda}\right)+\exp\left(-i2\pi m\frac{r}{\Lambda}\right)\right]. \quad (3)$$

Note that these two power expressions in the square bracket essentially denote the transmission functions of an axicon pair: a negative axicon and the other positive one [51]. The coefficient a_m can be rewritten as

$$a_m=c_m+c_{-m}=|c_m|\exp\left(i\frac{\Delta\phi_m}{2}\right)+|c_{-m}|\exp\left(-i\frac{\Delta\phi_m}{2}\right), \quad (4)$$

where $c_{\pm m}=\frac{1}{2}\int_0^{\Lambda}T(r)\exp(\mp i2\pi mr/\Lambda)\mathrm{d}r$, with $\Delta\phi_m=|\arg\{c_m\}-\arg\{c_{-m}\}|$ being the phase delay between these two coefficients and $|c_{\pm m}|$ being their amplitudes. For binary $(0,\pi)$ pure-phase gratings, $|c_{+m}|=|c_{-m}|$, and the mth order can be rewritten further as

$$h_m(r,\theta)=\sum_{m=1}^{\infty}|c_m|\cos\left(2\pi m\frac{r}{\Lambda}+\Delta\phi_m/2\right)\exp(il\theta), \quad (5)$$

where the coefficient can be expressed as

$$c_m = \sum_{n=1}^{N-1} \int_{r_n}^{r_{n+1}} \exp\left\{ i \frac{[1+(-1)^n]\pi}{2} \right\} \exp\left(i2\pi m \frac{r}{\Lambda} \right) \mathrm{d}r, \quad (6)$$

with $\{r_n\}$ being the normalized transitional points in one period along the radial direction of a binary $(0, \pi)$ pure-phase circular grating, which is also called a circular Dammann grating, and N being the total number of transitional points in one period. Then the Fraunhofer diffraction field of the mth non-zeroth order can be written as

$$H_m(\rho, \varphi) = (-i)^{l+1} \frac{k}{f} \exp(il\varphi)[u_m H_m^c(\rho) + v_m H_m^s(\rho)], \quad (7)$$

where

$$H_m^c(\rho) = \int_0^R \cos(2\pi m r/\Lambda) J_l(k\rho r/f) r \mathrm{d}r, \quad (8a)$$

$$H_m^s(\rho) = \int_0^R \sin(2\pi m r/\Lambda) J_l(k\rho r/f) r \mathrm{d}r. \quad (8b)$$

The Fourier spectrum of the mth-order circular cosine function embedded with a spiral phase expressed in Eq. (7) is essentially a weighted sum of two impulse rings (see details in Appendix A) with coefficients of $u_m = \cos(\Delta\phi_m/2)$ and $v_m = -\sin(\Delta\phi_m/2)$. Thus, we can control the ring profiles of POVs by changing the phase delay $\Delta\phi_m$ determined by the grating structure. Given a phase delay $\Delta\phi_m$, one can determine the side-lobe ratio (defined as the ratio of peak intensities of the brightest lobe ring to the main ring) as

$$\beta(\Delta\phi_m) = \begin{cases} |H_m^{\min}/H_m^{\max}|^2, & \text{if } |H_m^{\max}| \geq |H_m^{\min}| \\ |H_m^{\max}/H_m^{\min}|^2, & \text{if } |H_m^{\max}| < |H_m^{\min}| \end{cases}, \quad (9)$$

where $H_m^{\min}$ and $H_m^{\max}$ are the minimum and maximum values of the radial diffraction field of the mth order described in Eq. (7), respectively. According to this equation, one can control the side-lobe ratio by changing the phase delay $\Delta\phi_m$, which is determined by the grating structure. Thus, one can control the radial intensity profile of impulse rings of POVs just by changing the grating structure. For example, an "absolute" dark ring surrounded by two bright lobe rings in each side could be expected due to destructive interference when the side-lobe ratio is equal to 1. Then the whole design flow for generation of POVs with controllable ring profiles can be divided into four steps as follows.

(1) Determining the period number inside the aperture and the side-lobe ratio of the ring profile along the radial direction, and choosing the topological charge according to application requirements.

(2) Calculating the target phase delay according to Eqs. (7)–(9). Then searching for transitional points in each period of the CDG by minimizing the difference between the target phase delay and the actual phase difference between the axicon pair corresponding to the mth order of the CDG.

(3) By using the transitional points obtained in step (2) as initial solutions, optimizing further transitional points by minimizing the difference between the actual side-lobe ratio and the target value and maximizing the feature size (defined as the finest linewidth of the structure of CDGs) with a suitable weight factor between these two optimization criteria.

(4) After the transitional points are determined, one can obtain the grating structure by assigning those concentric rings periodically along the radial direction with the chosen period number.

It should be noted that, in theory, one could design a CDG for generation of POVs at any high diffraction order, and it is also possible to achieve multiple concentric impulse rings of POVs [50]. Here we just set the order as $m = 1$ in practice, and thus a single impulse ring will be expected, similar to traditional POVs. Furthermore, the integrals in Eqs. (8a) and (8b) will approach the lth-order Hankel transform of circular cosine and sine functions expressed in Eqs. (A7) and (A8) (see Appendix A), when the aperture size R is large enough. However, in practice, it is impossible to obtain an infinitely large aperture, and the limited aperture size determines that the period number inside the aperture is also limited. When the period number inside the aperture is not large enough, the phase delay is sensitive to the period number, and thus we need to reoptimize the grating structure when the period number is different.

B. Experimental Scheme

In order to verify the designed gratings embedded with vortices, we design a proof-of-principle experiment setup as shown in Fig. 1 for investigation of those generalized POVs. An expanded and collimated laser beam operating at 532 nm

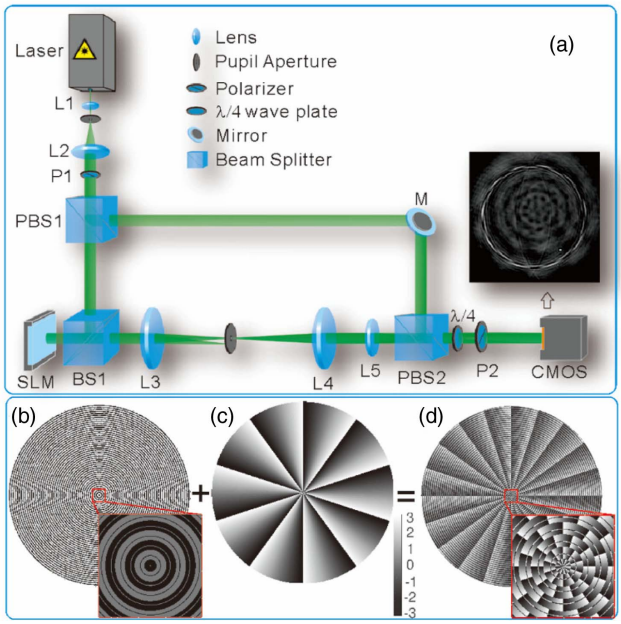

Fig. 1. Schematic diagrams of the experimental scheme. (a) The proof-of-principle experimental setup. L1 ~ 2 are lenses for expanding and collimation. L3 and L4 are a confocal lens pair, and L5 is the focusing lens; PBS1 ~ 2 are polarizing beam splitter cubes; BS1 is a non-polarizing beam splitter; M is a reflective mirror; SLM denotes a spatial light modulator; P1 ~ 2 denote polarizers; $\lambda/4$ denotes a quarter-wave plate. CMOS denotes a complementary metal-oxide semiconductor camera. (b) Phase distributions of a typical binary CDG, (c) a spiral phase, and (d) the CDG embedded with the spiral phase. The insets in the bottom-right corner indicate the enlarged portions in those rectangular areas in (b) and (d), respectively.

(Coherent Verdi 6) is used as the light source. The collimated beam passes through a polarizer P1, and then it is divided into two paths by a polarizing beam splitter cube PBS1. The transmitted path is horizontally polarized (p polarization), and it is directed by a non-polarizing beam splitter cube BS1 onto the liquid-crystal display (LCD) of a programmable spatial light modulator (SLM, HoloEye, Pluto NIR-011, pixel size 8 μm, and 1080 × 1920 pixels), where the phase of the CDGs embedded with a spiral phase encoded into a blazed grating is loaded. Next, the modulated beam is reflected back from the LCD, and then it is relayed by a confocal lens pair L3 and L4 with a tunable iris for singling out the first diffraction order, which carries the designed phase of the CDGs embedded with spiral phases. The filtered field is then focused by a converging lens L5 with focal length of 600 mm, and a CMOS camera (Edmund Optics, EO2323M, pixel size 4.8 μm, and 1200 × 1920 pixels) is located in the back focal plane of lens L5 to detect the intensity field. Another path is vertically polarized (s polarization), and it is reflected by a reflective mirror M. Then this reference path is finally combined with the first aforementioned path by another polarizing beam splitter cube PBS2, the interference field passes a $\lambda/4$-wave plate with a fast axis of $\pi/4$ rad and a polarizer P2, and then it is detected by the CMOS camera. Care must be taken to adjust the distance between lenses L1 and L2 to make sure that the expanded beam is free of spherical aberrations. A homemade shearing interferometer is used here to examine the transmitted wavefront. Besides the interference fields, the focused field of the generated POVs on the focal plane is also captured by the CMOS camera when the reference beam is blocked.

3. RESULTS AND DISCUSSION

A. Dark Perfect Optical Vortices

As pointed out above, one can control the ring profile by changing the phase delay between those two impulse rings (through the change of the grating structure). One important case is that a dark ring surrounded by two bright lobe rings on each side could be realized when destructive interference is achieved between those inward- and outward-oriented impulse rings. Here, as examples, we design three type of CDGs embedded with spiral phases for generation of dark POVs with charges of $l = 1$, −5, and 15, and the period number inside the aperture is always set to be 20 in the following unless otherwise specified. The normalized transitional points $\{r_n\}$ in the first half-period of these three CDGs are {0.36309, 0.48272}, {0.26388, 0.44996}, and {0.28769, 0.47858}. The phase distribution in the last half-period is inversed, and thus those normalized transitional points along the radial coordinate can be derived by $\{r_n + 0.5\}$ [52].

Figure 2 illustrates the experimental results of these three POVs with dark rings, compared with their simulation results. It is seen clearly that dark POVs are all well generated as expected. Moreover, from those intensity profiles along the dotted line crossing the center, one can also see that the valleys of these dark rings are always kept low enough for all cases, which suggests that the sharpness of these dark POVs is almost independent of the topological charge. Furthermore, the interference fringes between these POVs and plane waves are also shown.

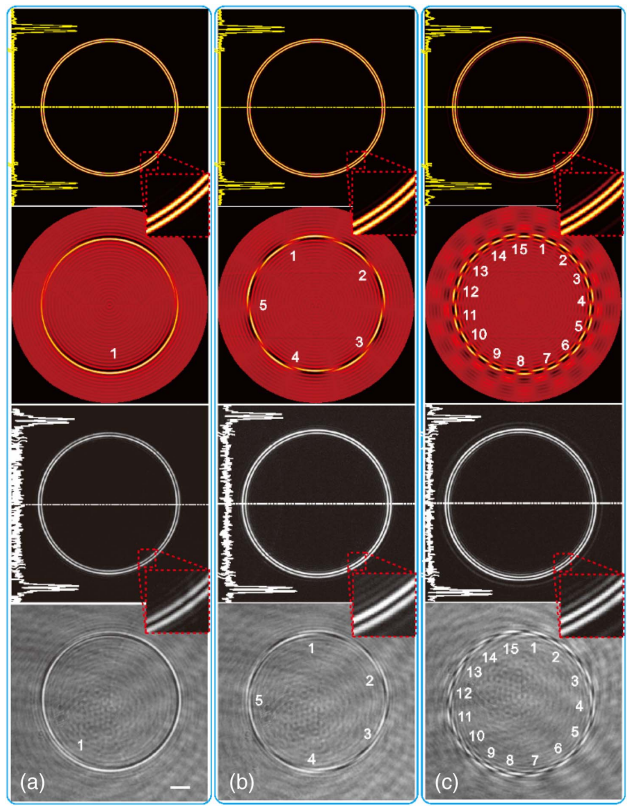

Fig. 2. Simulation and experimental results of dark POVs generated by CDGs embedded with spiral phases with charges of (a) $l = 1$, (b) −5, and (c) 15. In each box, the simulation results of the intensity distribution and interferograms are shown in the first and second rows; the experimental results of the intensity distribution and interferograms are shown in the third and fourth rows, respectively. The insets are enlarged portions of dark impulse rings in rectangular areas in those sub-images for intensity distribution. The scale bar denotes 300 μm.

It is seen that those interferograms are characterized by petal-like patterns, and each interferogram possesses an l-fold rotational symmetry. In addition, the amplitude of topological charges can be figured out based on the petal-like patterns, and it is l if the number of those petals is $2l$. It is indicated that, according to this rule, the amplitudes of topological charges carried by these dark POVs are 1, 5, and 15, which is in good agreement with theoretical predictions. Note that interference fringes on the focal plane are l-fold rotational symmetric, and one could not easily identify the sign of the topological charge from those interferograms on the focal plane. However, the sign can be identified by checking the rotational direction of the interference fringes on the defocused planes. Those petal-like patterns will become a series of helices on the defocused planes, and the sign of the topological charge can be identified by the rotational direction of those helices. Figure 3 shows the simulation and experimental results of the interference fringes on defocused planes for two dark POVs with charges of $l = 10$ and $l = -5$. It is clearly shown that the helix-type fringes are obtained as predicted, and the sign of the topological charge can be identified by the chirality of the helices. For those interferograms on the defocused plane

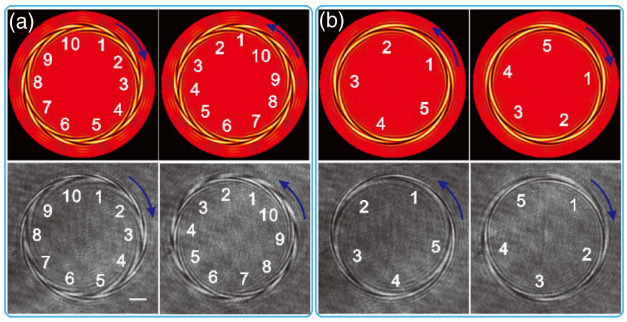

Fig. 3. Simulation and experimental results of interferograms on defocused planes (with defocus distance $\Delta d = 10$ mm) for dark POVs with charges of (a) $l = 10$ and (b) −5. In each box, the simulation and experimental results are shown in the first and second rows, and the results on defocused planes before and after the focus are shown in the first and second columns, respectively. The scale bar denotes 300 μm.

before the focus, the clockwise helices indicate a positive charge, while the anticlockwise helices suggest a negative one, and the rotational directions of those helices are inversed for those interferograms on defocused planes after the focus.

In order to further verify the generated vortices, the phase distributions of dark POVs with charges of $l = 10$ and $l = -5$ on defocused planes (defocus distance is about $\Delta d = 25$ mm) are extracted by six-step phase-shifted interferograms as shown in Fig. 4. By rotating the transmission axis of polarizer P2 at six different angles with a constant step of $\pi/6$ rad, one can extract the phase on the defocused planes using those six phase-shifted interferograms (see details in Appendix B). From this figure, it is seen clearly that the amplitudes of topological charge are $|l| = 10$ and $|l| = 5$ for these two dark-ring POVs, respectively. Furthermore, one can also see that the anticlockwise phase gradient direction indicates a positive charge ($l = 10$), while the clockwise one suggests a negative charge ($l = -5$). It should be pointed out that the gradient of the extracted phase is not perfectly linear along the azimuthal coordinate, which is predominately caused by mechanical vibrations, air

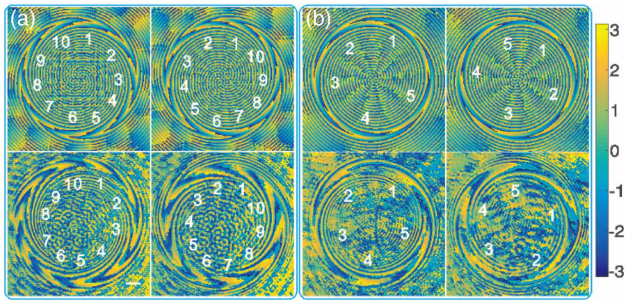

Fig. 4. Simulation and experimental results of phase distributions on defocused planes (with defocus distance $\Delta d = 25$ mm) for dark POVs with charges of (a) $l = 10$ and (b) $l = -5$. In each box, the simulation and the experimental results are shown in the first and second rows, and the results on defocused planes before and after the focus are shown in the first and second columns, respectively. The scale bar denotes 300 μm.

disturbances, temperature fluctuations, and also instability of the laser source.

Therefore, the type of dark POVs surrounded by two bright lobe rings on each side proposed here is an "absolute" dark ring due to destructive interference, which provides an annular potential well along the dark impulse ring. This annular potential well could be used for trapping low-index particles, cells, or quantum gases and transferring OAM carried by those dark POVs to trapped targets. Different from the method proposed by Liang *et al.* [43], this scheme proposed here is essentially the coherent superposition of two impulse rings, an inside-oriented one and the other outside-oriented one. Thus, one can tune the ring profile by changing the phase delay between those two impulse rings. As demonstrated by Liang *et al.*, there is residual non-zero intensity in the dark ring generated by their scheme. Moreover, the residual non-zero valley is higher for larger topological charge, which indicates that the sharpness of the potential well will degenerate for those POVs with large topological charge. The dark POVs proposed here could totally overcome this drawback.

B. Bright Perfect Optical Vortices

It is straightforward that, besides the dark POVs, one can also obtain bright POVs by choosing a phase delay resulting in constructive interference. In this case, the side-lobe ratio reaches its minimum value by optimizing the structure of the CDGs. Figure 5 illustrates simulation and experimental results of another three bright POVs with topological charge of $l = 1$, −5, and 20 generated by CDGs embedded with spiral phases. The normalized transitional points $\{r_n\}$ in the first half-periods of these three CDGs are {0.14655, 0.46455}, {0.07592, 0.48340}, and {0.029716, 0.48696} for those three bright POVs. It is seen that a bright impulse ring accompanied by weak lobe rings is well generated as predicted, with the consideration of various errors, such as alignment errors, phase errors induced by imperfect gamma correction of the SLM, and also various residual aberrations of the focusing system. In this case, the number of bright petals in interferograms on the focal plane indicates the amplitude of the topological charge, and the sign can be identified by checking the rotational direction of interference helices on defocused planes, similar to the aforementioned dark POVs. It should be noted that the side-lobe ratio increases with the topological charge, which will be discussed further in the following.

C. Perfect Optical Vortices with a Controllable Ring Profile

It has been shown that one can control the ring profile by changing the weight coefficient through choosing the corresponding phase delay, since the Fourier spectrum of each diffraction order is essentially a weighted sum of two impulse rings. In this part, we will demonstrate that the ring profile can be continuously adjusted by changing the grating structure of CDGs. As examples, we design a POV with charge of $l = 10$ with six different ring profiles, gradually ranging from a dark ring to a bright ring, within a whole transition cycle [the phase delay $\Delta\phi_m$ in Eq. (9) is ranged from 0 to 2π]. Figure 6 shows a typical curve of the side-lobe ratio versus the phase delay under the condition of charge $l = 10$ and period number inside the

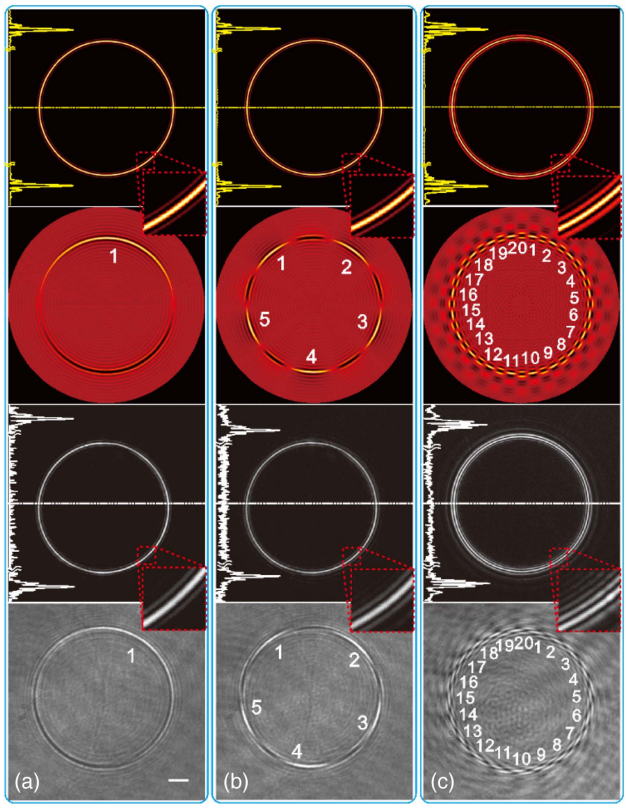

Fig. 5. Simulation and experimental results of bright POVs generated by CDGs embedded with spiral phases with charges of (a) $l = 1$, (b) −5, and (c) 20. In each box, the simulation results of the intensity distributions and interferograms are shown in the first and second rows; the experimental results of the intensity distributions and interferograms are shown in the third and fourth rows, respectively. The insets are enlarged portions of bright impulse rings in rectangular areas in those sub-figures for intensity distribution. The scale bar denotes 300 μm.

aperture of $N = 30$. From this figure, one can see clearly how the side-lobe ratio is influenced when the phase delay $\Delta\phi_m$ is gradually varied in the range of $[0, 2\pi]$. It can be seen that, when $\Delta\phi_m = 0$, the side-lobe ratio is 0.41, and a single bright ring accompanied by a relatively weak lobe ring outside is generated. When $\Delta\phi_m$ continues to increase, the side-lobe ratio starts to decrease, and then it reaches its minimum value of 0.28 at $\Delta\phi_m = 0.2122\pi$. In this case, the Hankel spectrum is the result of constructive interference of those inward- and outward-oriented impulse rings, and thus a bright ring is obtained at the mth order. Actually, this case is the best solution of POVs for side-lobe suppression. Then, when $\Delta\phi_m$ increases further, the side-lobe ratio starts to increase gradually to its maximum value at the point of $\Delta\phi_m = 1.3499\pi$. This time, the spectrum is the result of destructive interference of those inward- and outward-oriented impulse rings, and thus a dark ring surrounded by two bright lobe rings is generated. When $\Delta\phi_m$ continues to increase until it reaches 2π, the side-lobe ratio decreases and at last it reaches its initial value again. Up to now, a full cycle of evaluating the ring profile of the impulse spectrum of the mth order was discussed when the phase delay $\Delta\phi_m$ is gradually varied from 0 to 2π. Here, as examples, six different POVs (with charge of $l = 10$) with different ring profiles are also shown in Fig. 6. It is shown that an impulse ring with side-lobe ratio of 1/3 with a lobe ring outside, 1/3 with a lobe ring inside, 2/3 with a lobe ring inside, 2/3 with a lobe ring outside, and also a bright and a dark POV, could be achieved when phase delay is $\Delta\phi_m = 0.1204\pi$, 0.3733π, 1.0095π, 1.663π, 0.2122π, and 1.3499π, respectively. After further optimization, the normalized transitional points $\{r_n\}$ in the first half-period for those CDGs are {0.03723, 0.23090}, {0.06364, 0.20280}, {0.04368, 0.45274}, {0.32144, 0.47779}, {0.01662, 0.20280}, {0.38419, 0.46847} for those six POVs with different ring profiles, respectively. It is seen explicitly that one could control the ring profile of POVs by changing the phase delay, which is finally determined by the grating structure of the CDGs, and an impulse ring with side-lobe ratio of 1/3 with a lobe ring outside, 1/3 with a lobe ring inside, 2/3 with a lobe ring inside, 2/3 with a lobe ring outside, and also a bright and a dark POV, is well generated as predicated. The interferograms on the focal planes indicate that those POVs carry topological charge of $l = 10$. A much more subtle transition from a bright POV to a dark one and then again to a bright POV is demonstrated in Visualization 1. Up to now, we have demonstrated that a type of generalized POVs with a controllable ring profile could be well generated as expected. Thus, the method proposed here opens an avenue for controllable tuning of the ring profile of POVs by changing the structure of CDGs.

D. Characterization of Generated Perfect Optical Vortices

In this section, we will discuss how the performance parameters of POVs generated by CDGs embedded with spiral phases are influenced by the topological charge and period number, which include ring size, ring width, and also side-lobe ratio. Figure 7 shows experimental and simulation results of these influences. It can be seen from Fig. 7(a) that the ring size increases with the topological charge both for bright and dark POVs, and the increment is much smaller than that of its ring radius. So, similar to those all "perfect" optical vortices reported in the past [53,54], the POVs proposed here are also only quasi-perfect in the strict sense [55]. The influence of topological charge on the ring width is shown in Fig. 7(b), from which one can see that the ring width decreases slightly with the charge for bright POVs, while those ring widths for dark POVs are nearly invariable. Further, the ring width of the dark POVs is smaller than that of bright POVs. Figure 7(c) shows the side-lobe ratios versus the topological charge. It is seen that the side-lobe ratios are all nearly unity for those dark POVs, which indicates that the dark POVs are of high quality. However, those side-lobe ratios increase with the charge for those bright POVs. Figures 7(d)–7(f) show the ring radii, ring width, and side-lobe ratio versus the period number inside the focusing aperture. It is shown that the ring radius is linearly increased with the period number both for bright and dark POVs. One can also see from Fig. 7(e) that the ring widths are nearly constant with the increase of the period number. It should be noted that the side-lobe ratios for those bright POVs decrease with the period number, while those of dark

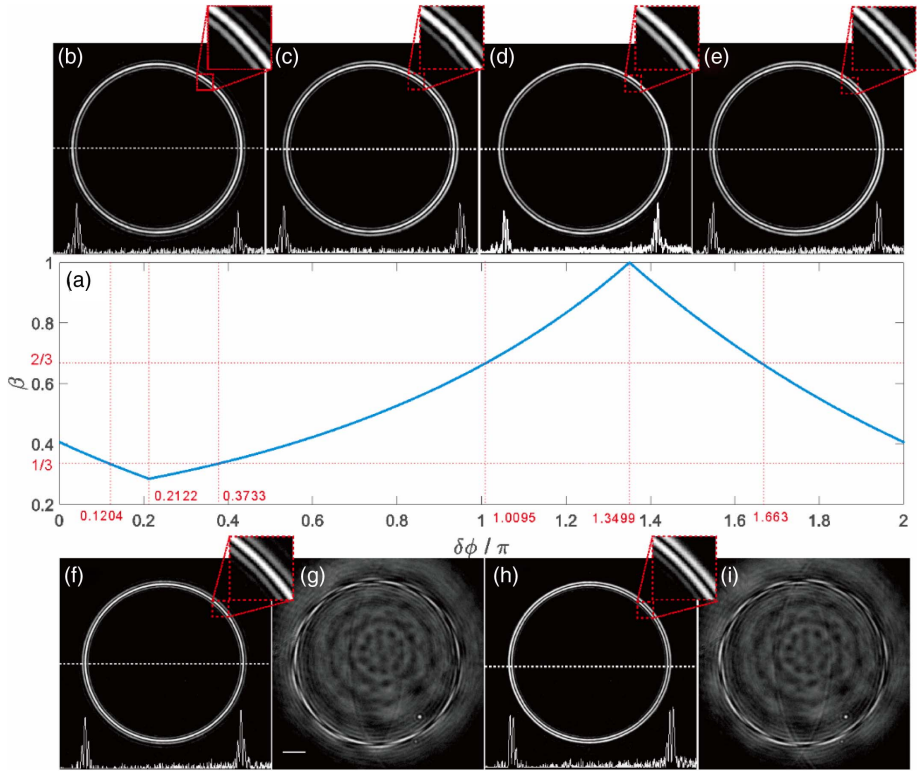

Fig. 6. Simulation and experimental results of POVs with tunable ring profiles generated by CDGs (with period number of $N = 30$ inside the aperture) embedded with spiral phase with charge of $l = 10$. (a) The curve of the side-lobe ratio β as a function of the phase difference $\delta\phi$; a POV with side-lobe ratio of (b) 1/3 with a lobe ring outside, (c) 1/3 with a lobe ring inside, (d) 2/3 with a lobe ring inside, and (e) 2/3 with a lobe ring outside; (f) a POV with a bright ring profile (a bright POV with the smallest side-lobe ratio), and (g) denotes its interferogram on the focal plane; (h) a POV with a dark ring profile (a dark POV with unity side-lobe ratio), and (i) is its interferogram on the focal plane. The scale bar denotes 500 μm.

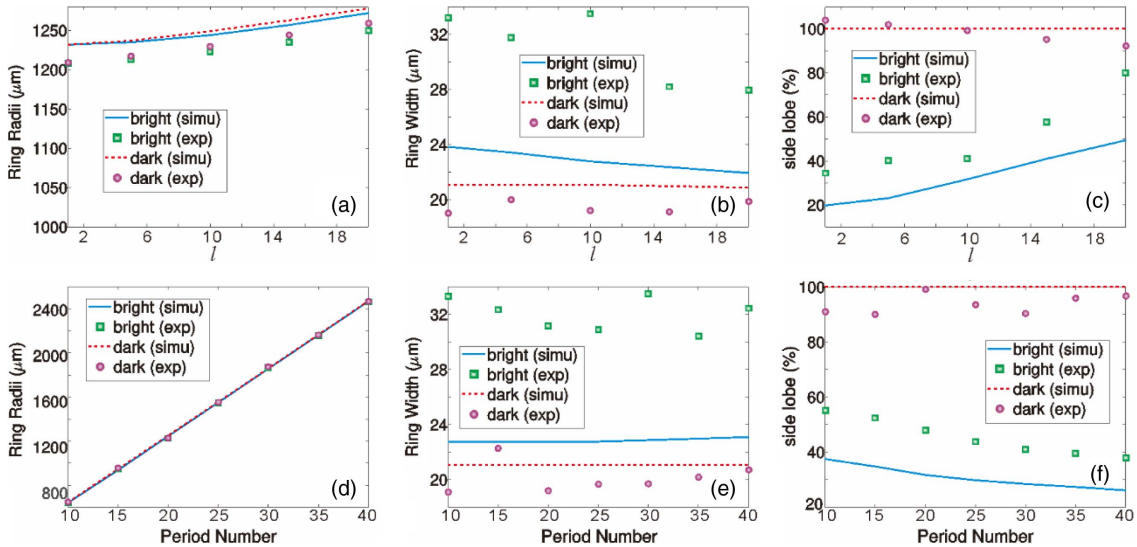

Fig. 7. Influences of topological charge and period number on performance parameters of POVs with bright and dark ring profiles generated by CDGs. (a) The ring radius, (b) the ring width, and (c) the side-lobe ratio as a function of the charge; (d) the ring radius, (e) the ring width, and (f) the side-lobe ratio versus the period number inside the aperture. In each sub-figure, the blue solid line denotes the simulation results of POVs with bright ring profiles (bright POVs) and the red broken line denotes the simulation results of POVs with dark ring profiles (dark POVs); the square denotes the experimental results of bright POVs, and the circle is the experimental results of dark POVs.

POVs are nearly invariable. It suggests that one can effectively reduce the side lobe by increasing the period number inside the focusing lens. In addition, it is noted that experimental results of the ring width of bright POVs are almost always larger than theoretical predictions, while the situation is reversed for dark POVs. Also, the side-lobe ratios of bright POVs in experiments are always larger than the theoretical ones. These deviations are mainly caused by residual aberrations. On the other hand, those disagreements between theoretical and experimental values of the ring radii are predominantly attributed to the deviation of the focal length of the converging lens L5. Moreover, the non-zero background noise that is induced by environmental light and also dark current of the camera also contributes to all these errors.

4. CONCLUSION AND OUTLOOK

POVs enable one to overcome the limitation caused by strong dependence of the ring diameter on the topological charge for conventional optical vortices. However, in the past, POVs were all shaped into bright rings with a single main lobe in the radial intensity profile. Here a method based on modulated circular sine/cosine functions is proposed for enhanced control of the ring profile of POVs, especially a type of "absolute" dark POVs, and is demonstrated. As examples, several dark POVs are presented, and the experimental results agree well with theoretical predictions. The interference field can be used for detecting topological charges. Also, this method can be used for generation of conventional bright POVs, and several examples are demonstrated theoretically and experimentally. It is shown that bright impulse rings can be well generated compared with other reported schemes. In addition, a POV with a controllable ring profile is demonstrated. It should be noted that, similar to those all "perfect" optical vortices reported in the past, the POVs proposed here are also only quasi-perfect in the strict sense. Moreover, it is shown that the side-lobe ratio for bright POVs decreases with the period number, which suggests that one could effectively reduce the side lobe by increasing the period number inside the lens aperture. Therefore, this type of more generalized POVs opens up new possibilities to controllably tune the ring profile of perfect vortices; this type of novel perfect vortices will enrich the content of the attractive subject of singular optics, and it should be of high interest for its potential in a range of applications such as optical manipulations, optical communications, enhanced optical imaging, and also novel structured pumping lasers. Recently, micro-/nano-cavity lasers, especially micro-/nano-ring lasers, are attracting considerable interest for their high quantum yields, tunable emission wavelength, and easy integration [56]. The impulse ring proposed here could be an optimal option for pumping those micro-/nano-ring lasers.

APPENDIX A: THEORY OF THE HANKEL TRANSFORM FOR CIRCULAR GRATINGS

It is known that the transmission function of a circular grating with a radial periodic property can be decomposed into a series of circular cosine or sine functions with different frequencies [45,46]. The 2D Fourier transform (also called the zeroth-order Hankel transform) of the circular cosine/sine functions can be written as

$$\cos(\alpha r) \overset{\mathcal{H}}{\leftrightarrow} \frac{\alpha}{2}\frac{1}{(\alpha/2+\pi\rho)^{3/2}}\delta^{(1/2)}(\alpha/2\pi-\rho), \tag{A1}$$

$$\sin(\alpha r) \overset{\mathcal{H}}{\leftrightarrow} \frac{\alpha}{2}\frac{1}{(\alpha/2+\pi\rho)^{3/2}}\delta^{(1/2)}(\rho-\alpha/2\pi), \tag{A2}$$

where α is the scale parameter that determines the diameter of the impulse ring, ρ is the radial coordinate in the Fourier plane, and $\delta^{1/2}(\cdot)$ denotes the half-order derivative Dirac delta function. These two equations reveal the impulse behavior of the Fourier spectrum of circular sine and cosine functions. Among them, the two impulse rings $\delta^{1/2}(\alpha/2\pi-\rho)$ and $\delta^{1/2}(\rho-\alpha/2\pi)$ represent an inward-oriented impulse ring and the other outward-oriented one, respectively. When a phase shift $\Delta\phi$ is introduced, a more generalized form of a circular cosine or sine function can be expressed as

$$\cos\left(\alpha r+\frac{\Delta\phi}{2}\right) = u\cos(\alpha r)+v\sin(\alpha r), \tag{A3}$$

$$\sin\left(\alpha r+\frac{\Delta\phi}{2}\right) = -v\cos(\alpha r)+u\sin(\alpha r), \tag{A4}$$

where the two weight coefficients are $u=\cos(\Delta\phi/2)$ and $v=-\sin(\Delta\phi/2)$. It means that the phase-shifted circular sine or cosine function can be expressed by a weighted sum of a pair of circular cosine and sine functions. For brevity, we only discuss the case of circular cosine functions in the following. According to Eqs. (A1), (A2), and (A3), the Fourier transform of a phase-shifted circular cosine function can be written as [57]

$$\begin{aligned}&\mathcal{H}\left\{\cos\left(\alpha r+\frac{\Delta\phi}{2}\right)\right\}\\&=\frac{\alpha}{2}\frac{1}{(\alpha/2+\pi\rho)^{3/2}}\\&\quad\times\left[u\delta^{1/2}\left(\rho-\frac{\alpha}{2\pi}\right)+v\delta^{1/2}\left(\frac{\alpha}{2\pi}-\rho\right)\right],\end{aligned} \tag{A5}$$

where $\mathcal{H}\{\cdot\}$ denotes the zeroth-order Hankel transformation. It is seen from this equation that the Fourier spectrum of a phase-shifted circular cosine function essentially denotes a weighted sum of the spectra of circular cosine and sine functions. Furthermore, when another spiral phase with topological charge of l is introduced, the Hankel spectrum of a circular cosine function can be derived as

$$\begin{aligned}\mathcal{H}\left\{\cos\left(\alpha r+\frac{\Delta\phi}{2}\right)e^{il\theta}\right\} &= 2\pi e^{il\varphi}\int_0^\infty[u\cos(\alpha r)\\&\quad+v\sin(\alpha r)]J_l(2\pi\rho r)r\mathrm{d}r\\&=2\pi e^{il\varphi}[uH_c(\rho)+vH_s(\rho)],\end{aligned} \tag{A6}$$

where the integrals H_c and H_s can be written as the lth-order Hankel transform of circular cosine and sine functions, respectively, and these two integrals can be written in the form of piecewise functions as [58]

$$H_c(\rho)=\int_0^{\infty}\cos(\alpha r)J_l(2\pi\rho r)r\mathrm{d}r=\begin{cases}\frac{(2\pi\rho)^l\Gamma(l+2)\cos[\pi(l+2)/2]}{2^l\alpha^{(l+2)}\Gamma(l+1)}{}_2F_1[1+l/2,3/2+l/2;l+1;(2\pi\rho/\alpha)^2], & 0<\rho<\alpha/2\pi\\ \frac{\Gamma(l/2+1)}{2(\pi\rho)^2}\Gamma(l/2){}_2F_1[1+l/2,1-l/2;1/2;(\alpha/2\pi\rho)^2], & \rho>\alpha/2\pi\end{cases},\tag{A7}$$

$$H_s(\rho)=\int_0^{\infty}\sin(\alpha r)J_l(2\pi\rho r)r\mathrm{d}r=\begin{cases}\frac{(2\pi\rho)^l\Gamma(l+2)\sin[\pi(l+2)/2]}{2^l\alpha^{(l+2)}\Gamma(l+1)}{}_2F_1[3/2+l/2,1+l/2;l+1;(2\pi\rho/\alpha)^2], & 0<\rho<\alpha/2\pi\\ \frac{2^l\alpha\Gamma(l/2+3/2)}{2(\pi\rho)^3\Gamma(l/2-1/2)}{}_2F_1[3/2+l/2,3/2-l/2;3/2;(\alpha/2\pi\rho)^2], & \rho>\alpha/2\pi\end{cases},\tag{A8}$$

where $\Gamma(\cdot)$ denotes a gamma function and ${}_2F_1(a,b;c;x)$ is a hyper-geometric function. It indicates that there is a singularity at the position of $\rho=\alpha/2\pi$ for these two piecewise functions. It has been shown that these two piecewise functions essentially represent a pair of impulse rings: one impulse ring with a trailing wake inward and the other one with a trailing wake outward [45]. Therefore, the Fourier spectrum of the circular cosine function embedded with a spiral phase expressed in Eq. (A6) can be regarded as a weighted sum of two impulse rings with coefficients of $u=\cos(\Delta\phi/2)$ and $v=-\sin(\Delta\phi/2)$, which are determined only by the phase delay $\Delta\phi$. It is suggested that an impulse vortex ring, i.e., a POV, could be generated, and one can adjust the weights of those two impulse rings by changing the phase delay and finally control the intensity profile of the impulse rings of perfect vortices. It should be noted that the impulse ring would become a dark ring surrounded by two bright lobe rings on each side due to destructive interference of those inward- and outward-oriented impulse rings when those two coefficients have equal amplitude but opposite signs, i.e., $u_m=-v_m$.

APPENDIX B: PHASE RETRIEVAL FROM SIX-STEP PHASE-SHIFTED INTERFEROGRAMS

In the experiment, the p component is transmitted from the polarizing beam splitter PBS1, and it is modulated by the SLM. Then the modulated beam is reflected back and combined with the s-polarized path by another polarizing beam splitter PBS2. The two paths with crossed polarization are converted into a pair of circularly polarized beams with inversed chirality after passing through a quarter-wave plate with a fast axis of $\pi/4$ rad. Then the interference field after passing through polarizer P2 can be written as

$$I(x,y)=\frac{A_x^2}{2}+\frac{A_y^2}{2}+A_xA_y\cos[\phi(x,y)+2\theta],\tag{B1}$$

where A_x and A_y are the amplitudes of the two crossed polarized paths and $\phi(x,y)$ is the phase difference between them. θ is the oriented angle of polarizer P2. By rotating the transmission axis of polarizer P2 with a constant step of $\Delta\theta=\pi/6$ rad, we can obtain six phase-shifted interferograms. Then the phase $\phi(x,y)$ can be retrieved by [59]

$$\phi(x,y)=\begin{cases}\arctan(y/x)-\pi, & x>0 \quad \text{and} \quad y>0\\ \arctan(y/x), & x>0 \quad \text{and} \quad y<0\\ \arctan(y/x)+\pi/2, & x<0\end{cases},\tag{B2}$$

where

$$x=I_0-4I_2+3I_4,\quad y=-(3I_1-4I_3+I_5),$$

and

$$I_n=\frac{A_x^2}{2}+\frac{A_y^2}{2}+A_xA_y\cos[\phi(x,y)+2n\Delta\theta],$$
$$n=0,1,2,3,4,5,$$

where $\Delta\theta=\pi/6$ rad is the rotation step of polarizer P2. Then the phase carried by the POVs could be identified by the phase difference $\phi(x,y)$ only if the reference beam is well collimated and it can be regarded as a plane wave. It should be pointed out that another path also introduces the phase difference, i.e., the random phase difference caused by mechanical vibrations, air disturbances, temperature fluctuations, and also instability of the laser source. Here we recorded a series of interferograms by the CMOS camera (with frame rate 50 frames per second, and each video includes more than 1200 frames) instead by a single image for each step. For each video, those frames with contrast over a threshold are chosen as the effective images waiting for further processing. First, each effective frame is binarized. Next, those binarized images are summed up, and the summation is binarized again. Then we calculate the correlation coefficients between each binarized frame and the above binarized summation and choose the frame with the highest correlation coefficient as the interferogram for each step. Finally, the 2D phase is retrieved from those six phase-shifted interferograms according to Eq. (B2).

Funding. Bureau of Science and Technology for Development, Chinese Academy of Sciences (QYZDJ-SSW-JSC014); Shanghai Science and Technology Committee (17ZR1448100, 19DZ2291102, 19JC1415400).

Disclosures. The authors declare no conflicts of interest.

REFERENCES

1. J. F. Nye and M. V. Berry, "Dislocations in wave trains," Proc. R. Soc. Lond. A **336**, 165–190 (1974).
2. A. M. Yao and M. J. Padgett, "Orbital angular momentum: origins, behavior and applications," Adv. Opt. Photon. **3**, 161–204 (2011).

3. L. Allen, M. W. Beijersbergen, R. J. C. Spreeuw, and J. P. Woerdman, "Orbital angular momentum of light and the transformation of Laguerre-Gaussian laser modes," Phys. Rev. A **45**, 8185–8189 (1992).
4. S. W. Hell and J. Wichmann, "Breaking the diffraction resolution limit by stimulated emission: stimulated-emission-depletion fluorescence microscopy," Opt. Lett. **19**, 780–782 (1994).
5. M. Kamper, H. Ta, N. A. Jensen, S. W. Hell, and S. Jakobs, "Near-infrared STED nanoscopy with an engineered bacterial phytochrome," Nat. Commun. **9**, 4762 (2018).
6. Y. Roichman, B. Sun, Y. Roichman, J. Amato-Grill, and D. G. Grier, "Optical forces arising from phase gradients," Phys. Rev. Lett. **100**, 013602 (2008).
7. M. Woerdemann, C. Alpmann, M. Esseling, and C. Denz, "Advanced optical trapping by complex beam shaping," Laser Photon. Rev. **7**, 839–854 (2013).
8. G. Chen, X. Huang, C. Xu, L. Huang, J. Xie, and D. Deng, "Propagation properties of autofocusing off-axis hollow vortex Gaussian beams in free space," Opt. Express **27**, 6357–6369 (2019).
9. G. Molina-Terriza, A. Vaziri, J. Řeháček, Z. Hradil, and A. Zeilinger, "Triggered qutrits for quantum communication protocols," Phys. Rev. Lett. **92**, 167903 (2004).
10. N. Bozinovic, Y. Yue, Y. Ren, M. Tur, P. Kristensen, H. Huang, A. E. Willner, and S. Ramachandran, "Terabit-scale orbital angular momentum mode division multiplexing in fibers," Science **340**, 1545–1548 (2013).
11. A. E. Willner, "Vector-mode multiplexing brings an additional approach for capacity growth in optical fibers," Light Sci. Appl. **7**, 18002 (2018).
12. G. Foo, D. M. Palacios, and G. A. Swartzlander, "Optical vortex coronagraph," Opt. Lett. **30**, 3308–3310 (2005).
13. S. Fürhapter, A. Jesacher, S. Bernet, and M. Ritsch-Marte, "Spiral phase contrast imaging in microscopy," Opt. Express **13**, 689–694 (2005).
14. Y. Pan, W. Jia, J. Yu, K. Dobson, C. Zhou, Y. Wang, and T.-C. Poon, "Edge extraction using a time-varying vortex beam in incoherent digital holography," Opt. Lett. **39**, 4176–4179 (2014).
15. T. Yuan, Y. Cheng, H. Wang, Y. Qin, and B. Fan, "Radar imaging using electromagnetic wave carrying orbital angular momentum," J. Electron. Imaging **26**, 023016 (2017).
16. D. Gauthier, P. Ribič, G. Adhikary, A. Camper, C. Chappuis, R. Cucini, L. F. DiMauro, G. Dovillaire, F. Frassetto, R. Géneaux, P. Miotti, L. Poletto, B. Ressel, C. Spezzani, M. Stupar, T. Ruchon, and G. De Ninno, "Tunable orbital angular momentum in high-harmonic generation," Nat. Commun. **8**, 14971 (2017).
17. R. Géneaux, A. Camper, T. Auguste, O. Gobert, J. Caillat, R. Taieb, and T. Ruchon, "Synthesis and characterization of attosecond light vortices in the extreme ultraviolet," Nat. Commun. **7**, 12583 (2016).
18. M. Zuerch, C. Kern, P. Hansinger, A. Dreischuh, and C. Spielmann, "Strong-field physics with singular light beams," Nat. Phys. **8**, 743–746 (2012).
19. A. Denoeud, L. Chopineau, A. Leblanc, and F. Quere, "Interaction of ultraintense laser vortices with plasma mirrors," Phys. Rev. Lett. **118**, 033902 (2017).
20. J. Wang, M. Zepf, and S. G. Rykovanov, "Intense attosecond pulses carrying orbital angular momentum using laser plasma interactions," Nat. Commun. **10**, 5554 (2019).
21. S. Sasaki and I. McNulty, "Proposal for generating brilliant x-ray beams carrying orbital angular momentum," Phys. Rev. Lett. **100**, 124801 (2008).
22. Y. Chen, J. Li, K. Z. Hatsagortsyan, and C. H. Keitel, "γ-ray beams with large orbital angular momentum via nonlinear Compton scattering with radiation reaction," Phys. Rev. Lett. **121**, 074801 (2018).
23. R. Imai, N. Kanda, T. Higuchi, K. Konishi, and M. Kuwata-Gonokami, "Generation of broadband terahertz vortex beams," Opt. Lett. **39**, 3714–3717 (2014).
24. A. A. Sirenko, P. Marsik, C. Bernhard, T. N. Stanislavchuk, V. Kiryukhin, and S.-W. Cheong, "Terahertz vortex beam as a spectroscopic probe of magnetic excitations," Phys. Rev. Lett. **122**, 237401 (2019).
25. M. Uchida and A. Tonomura, "Generation of electron beams carrying orbital angular momentum," Nature **464**, 737–739 (2010).
26. A. J. Silenko, P. Zhang, and L. Zou, "Manipulating twisted electron beams," Phys. Rev. Lett. **119**, 243903 (2017).
27. L. Zhang and P. L. Marston, "Angular momentum flux of nonparaxial acoustic vortex beams and torques on axisymmetric objects," Phys. Rev. E **84**, 065601 (2011).
28. N. Jiménez, V. Romero-García, L. M. García-Raffi, F. Camarena, and K. Staliunas, "Sharp acoustic vortex focusing by Fresnel-spiral zone plates," Appl. Phys. Lett. **112**, 204101 (2018).
29. A. S. Ostrovsky, C. Rickenstorff-Parrao, and V. Arrizón, "Generation of the 'perfect' optical vortex using a liquid-crystal spatial light modulator," Opt. Lett. **38**, 534–536 (2013).
30. C. Brunet, P. Vaity, Y. Messaddeq, S. LaRochelle, and L. A. Rusch, "Design, fabrication and validation of an OAM fiber supporting 36 states," Opt. Express **22**, 26117–26127 (2014).
31. M. Chen, M. Mazilu, Y. Arita, E. M. Wright, and K. Dholakia, "Dynamics of microparticles trapped in a perfect vortex beam," Opt. Lett. **38**, 4919–4922 (2013).
32. R. Paez-Lopez, U. Ruiz, V. Arrizon, and R. Ramos-Garcia, "Optical manipulation using optimal annular vortices," Opt. Lett. **41**, 4138–4141 (2016).
33. S. G. Reddy, P. Chithrabhanu, P. Vaity, A. Aadhi, S. Prabhakar, and R. P. Singh, "Non-diffracting speckles of a perfect vortex beam," J. Opt. **18**, 055602 (2016).
34. C. Zhang, C. Min, L. Du, and X. C. Yuan, "Perfect optical vortex enhanced surface plasmon excitation for plasmonic structured illumination microscopy imaging," Appl. Phys. Lett. **108**, 201601 (2016).
35. N. A. Chaitanya, M. V. Jabir, and G. K. Samanta, "Efficient nonlinear generation of high power, higher order, ultrafast 'perfect' vortices in green," Opt. Lett. **41**, 1348–1351 (2016).
36. M. V. Jabir, N. A. Chaitanya, A. Aadhi, and G. K. Samanta, "Generation of 'perfect' vortex of variable size and its effect in angular spectrum of the down-converted photons," Sci. Rep. **6**, 21877 (2016).
37. A. Banerji, R. P. Singh, D. Banerjee, and A. Bandyopadhyay, "Generating a perfect quantum optical vortex," Phys. Rev. A **94**, 053838 (2016).
38. P. Li, Y. Zhang, S. Liu, C. Ma, L. Han, H. Cheng, and J. Zhao, "Generation of perfect vectorial vortex beams," Opt. Lett. **41**, 2205–2208 (2016).
39. S. Fu, C. Gao, T. Wang, S. Zhang, and Y. Zhai, "Simultaneous generation of multiple perfect polarization vortices with selective spatial states in various diffraction orders," Opt. Lett. **41**, 5454–5457 (2016).
40. Y. Liu, Y. Ke, J. Zhou, Y. Liu, H. Luo, S. Wen, and D. Fan, "Generation of perfect vortex and vector beams based on Pancharatnam-Berry phase elements," Sci. Rep. **7**, 44096 (2017).
41. A. A. Kovalev, V. V. Kotlyar, and A. P. Porfirev, "A highly efficient element for generating elliptic perfect optical vortices," Appl. Phys. Lett. **110**, 261102 (2017).
42. X. Li, H. Ma, C. Yin, J. Tang, H. Li, M. Tang, J. Wang, Y. Tai, X. Li, and Y. Wang, "Controllable mode transformation in perfect optical vortices," Opt. Express **26**, 651–662 (2018).
43. Y. Liang, M. Lei, S. Yan, M. Li, Y. Cai, Z. Wang, X. Yu, and B. Yao, "Rotating of low-refractive-index microparticles with a quasi-perfect optical vortex," Appl. Opt. **57**, 79–84 (2018).
44. Y. Liang, S. Yan, M. He, M. Li, Y. Cai, Z. Wang, M. Lei, and B. Yao, "Generation of a double-ring perfect optical vortex by the Fourier transform of azimuthally polarized Bessel beams," Opt. Lett. **44**, 1504–1507 (2019).
45. I. Amidror, "Fourier spectrum of radially periodic images," J. Opt. Soc. Am. A **14**, 816–826 (1997).
46. I. Amidror, "Fourier spectra of radially periodic images with a non-symmetric radial period," J. Opt. A **1**, 621–625 (1999).
47. C. Zhou, J. Jia, and L. Liu, "Circular Dammann grating," Opt. Lett. **28**, 2174–2176 (2003).
48. S. Zhao and P. S. Chung, "Design of a circular Dammann grating," Opt. Lett. **31**, 2387–2389 (2006).
49. U. Levy, B. Desiatov, I. Goykhman, T. Nachmias, A. Ohayon, and S. E. Meltzer, "Design, fabrication, and characterization of circular Dammann gratings based on grayscale lithography," Opt. Lett. **35**, 880–882 (2010).

50. J. Yu, J. Wu, C. Xiang, H. Cao, L. Zhu, and C. Zhou, "A generalized circular Dammann grating with controllable impulse ring profile," IEEE Photon. Technol. Lett. **30**, 801–804 (2018).
51. L. Niggl, T. Lanzl, and M. Maier, "Properties of Bessel beams generated by periodic gratings of circular symmetry," J. Opt. Soc. Am. A **14**, 27–33 (1997).
52. C. Zhou and L. Liu, "Numerical study of Dammann array illuminators," Appl. Opt. **34**, 5961–5969 (1995).
53. V. Arrizón, U. Ruiz, D. Sánchez-de-la-Llave, G. Mellado-Villaseñor, and A. S. Ostrovsky, "Optimum generation of annular vortices using phase diffractive optical elements," Opt. Lett. **40**, 1173–1176 (2015).
54. P. Vaity and L. Rusch, "Perfect vortex beam: Fourier transformation of a Bessel beam," Opt. Lett. **40**, 597–600 (2015).
55. J. Pinnell, V. Rodríguez-Fajardo, and A. Forbes, "How perfect are perfect vortex beams?" Opt. Lett. **44**, 5614–5617 (2019).
56. K. Rong, F. Gan, K. Shi, S. Chu, and J. Chen, "Configurable integration of on-chip quantum dot lasers and subwavelength plasmonic waveguides," Adv. Mater. **30**, 1706546 (2018).
57. I. Amidror, "The Fourier-spectrum of circular sine and cosine gratings with arbitrary radial phase," Opt. Commun. **149**, 127–134 (1998).
58. H. Bateman, *Tables of Integral Transforms* (McGraw-Hill, 1954).
59. Y. Surrel, "Design of algorithms for phase measurements by the use of phase stepping," Appl. Opt. **35**, 51–60 (1996).